Near wake of the X-Rotor vertical-axis wind turbine

Bensason, David; Sciacchitano, Andrea; Ferreira, Carlos

DOI
10.1088/1742-6596/2505/1/012040

Publication date
2023

Published in
Journal of Physics: Conference Series

Citation (APA)
Bensason, D., Sciacchitano, A., & Ferreira, C. (2023). Near wake of the X-Rotor vertical-axis wind turbine. *Journal of Physics: Conference Series*, *2505*(1), Article 012040. https://doi.org/10.1088/1742-6596/2505/1/012040

Journal of Physics: Conference Series

Near wake of the X-Rotor vertical-axis wind turbine

To cite this article: David Bensason *et al* 2023 *J. Phys.: Conf. Ser.* **2505** 012040

Near wake of the X-Rotor vertical-axis wind turbine

David Bensason[1], **Andrea Sciacchitano**[1], **Carlos Ferreira**[1]

[1]Faculty of Aerospace Engineering, Technical University of Delft, 2629 HS Delft, Netherlands

E-mail: `d.y.bensason@tudelft.nl`

Abstract. In the present study, the near wake of a novel vertical-axis wind turbine known as the X-Rotor is experimentally investigated. Particle image velocimetry is used to measure the phase-locked flowfield at several streamwise locations within the rotor's volume of rotation. The results show a clear impact of coned blades on the streamwise and axial induction fields as well as the local presence of vorticity structures. A notable counteraction of the average expansion of the wake in the axial direction is observed stemming from the shed and tip vorticity of the coned blades. As a result, an axial contraction and radial expansion in the wake can be observed across several phase and cross-stream combinations as well as a consistent asymmetry in streamwise flow. These results encourage the development and validation of numerical models that can account for the three-dimensional induction field of the X-Rotor as well as a further study into the far wake and farm-level installation of vertical-axis wind turbines.

1. Introduction

The development around offshore wind energy technology has gained the spotlight following the recent initiative by the EU to increase renewable energy consumption by 5% by 2030 [1]. Offshore wind deployment is increasing given the favorable wind resource experienced by seaward turbines and lower level of social-political and environmental restrictions of large-scale instillation [2]. Although the potential of offshore installation is well established, there are still several challenges. Top-heavy horizontal-axis wind turbine (HAWT) designs suffer from performance losses due to wave surges. Furthermore, operation and maintenance for offshore floating HAWT are difficult due to the elevated position of the instrumentation in the nacelle, further increasing the operational costs [3]. Hence, in the context of the EU target, offshore wind technology needs to be diversified to reduce the costs of its implementation.

Vertical-axis wind turbines (VAWT) have several advantages over their horizontal-axis counterparts, including lower levels of sound emission [4], the potential to achieve a higher power density [5, 6], and independence from wind direction [7, 8]. Furthermore, in the context of offshore deployment, VAWT have a lower center of gravity as their heavy instrumentation (gearbox and drive train) can be positioned at the bottom of the tower [9]. This yields a more stable structure and simplifies the operation and maintenance costs. Despite these advantages, large-scale commercial deployment of VAWTs is hindered due to challenges associated with self-starting and premature mechanical failure. In response to these shortcomings and the desire to decrease the capital and operational costs of offshore wind, a novel offshore wind turbine concept known as the "X-Rotor" has been introduced.

The X-Rotor [10] is a radical rethink of the traditional VAWT geometry which includes coned blades in the shape of an "X" with wingtip mounted HAWTs responsible for generating electrical power. Up to now, studies concerning the X-Rotor have been focused on the structural performance and cost expenditure modeling [11, 10], yielding results that suggest a potential cost of energy reduction of 20%. However, the impact of this coned blade geometry on the surrounding flowfield has yet to be investigated. This three-dimensional aspect will inflict a notable vertical component in the local induction field of the turbine. Consequently, the near and far wake dynamics will be affected, suggesting serious implications for farm-level aerodynamics, installation, and control strategies. This work is a first step towards experimentally quantifying the unique aerodynamics of the X-Rotor. The flowfield at several planes and phases within the turbine volume is measured using stereoscopic particle-image velocimetry. Measurements focus on the induction, near-wake, and tip effects of a scaled X-Rotor.

2. Methodology

2.1. Wind tunnel

Experiments were performed in the Open Jet Facility (OJF) at TU Delft Aerospace Engineering Laboratories, illustrated in Figure 1. The atmospheric closed-loop wind tunnel has an octagonal exit section of 2.85m × 2.85m with a contraction ratio of 3:1. A controlled streamwise velocity of $U_\infty = 4\text{m/s}$ is used throughout the experiment. The resulting jet stream is bound by shear layers with a semi-angle of 4.7° with turbulence intensities reported to be 0.5% within the testing region [12].

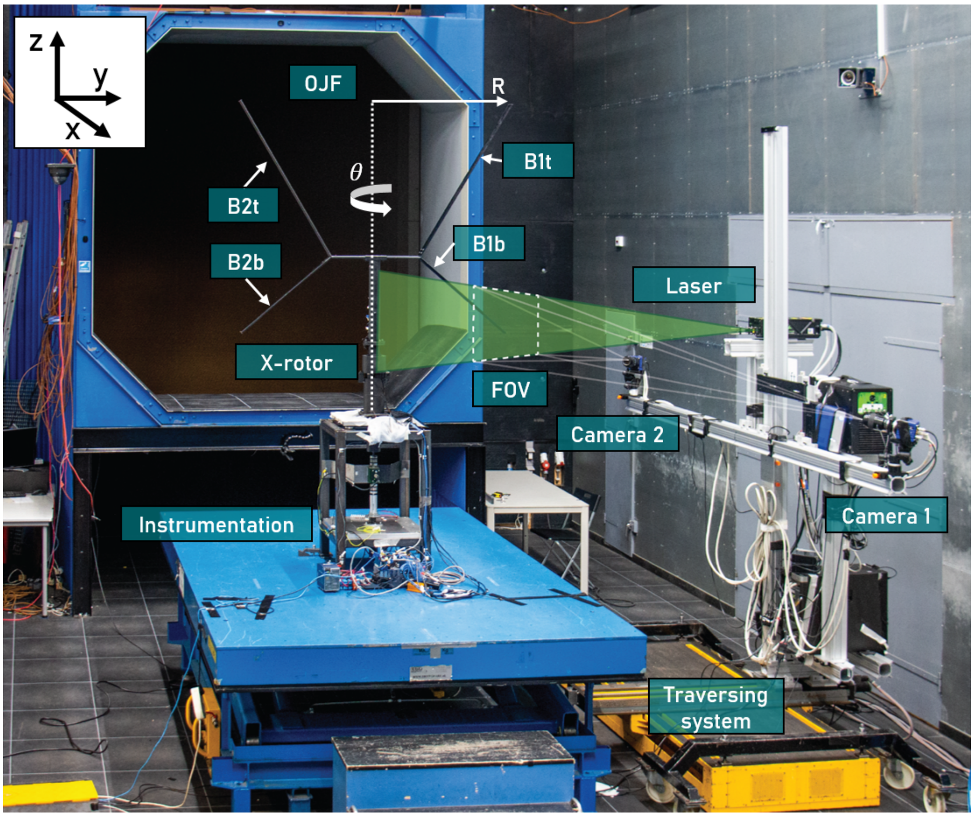

Figure 1: Experimental setup in the OJF wind tunnel at TU Delft. The main components of the setup and measurement systems are labeled. The direction of rotation and radius are marked for the X-Rotor model at phase $\theta = 0°$. A visualization of the illuminated measurement plane is provided with dashed lines enclosing the field of view (FOV).

2.2. Turbine model

A 1:100 scale X-Rotor model is mounted in the center of the test section. The model consists of four straight NACA0021 airfoils with a constant chord of c = 0.075m attached to a stiff crossbeam with the same profile and chord. Both the top and bottom blades have a tip radius of R = 0.75m and coning angles of 60° and 40°, respectively. Blades are marked, where 't' and 'b' denote top and bottom, respectively, and 1 and 2 denote the blades at phases $\theta = 0°$ and $\theta = 180°$, respectively. The model is mounted on a frame and driven at a constant tip-speed ratio of $\lambda = 4.0$, resulting in a chord-based Reynolds number of $Re_c = 8.1{\times}10^4$ at the tip. Instrumentation for measuring the shaft torque, rotational frequency, and turbine thrust vectoring is included in the frame. A detailed overview of the instrumentation is provided by LeBlanc et al. [13].

2.3. Flow measurement systems

A stereoscopic particle image velocimetry (PIV) system is used to measure several velocity fields at discrete planes in the wake. Seeding is generated via a SAFEX smoke generator with an average particle diameter of 1 µm. The particles are illuminated with a Quantel Evergreen double-pulsed Nd:YAG laser with a sheet thickness of approximately 4 mm. Finally, image pairs are captured at a frequency of 15 Hz using two LaVision sCMOS cameras shooting from opposing sides of the laser sheet. With a focal length of 105 mm, the resulting field of view (FOV) is approximately 43 cm × 30 cm, yielding a digital image resolution of 6 px/mm. The camera and laser systems are rigidly connected and mounted on a traversing system enabling a translation range in the x-axis and y-axis of 1.5 m and 0.5 m, respectively. Translation in the z-axis is achieved manually by shifting the rigid connection between the systems. Finally, results are processed with a cross-correlation-based image interrogation algorithm with window deformation, with window sizes of 64 px × 64 px and an overlap factor of 75 %.

2.4. Case description

The aforementioned measurement system captures phase-locked measurements of the flowfield at varying locations of the X-Rotor induction field, visualized in Figure 2. As defined in Figure 1, the coordinate system is such that x, y, and z are the streamwise, radial, and axial directions, respectively. The case of $x = 0$ corresponds to the center of the turbine tower in the streamwise direction and a phase of $\theta = 0°$ when both blades lie on the $x = 0$ plane. The normalized cross-stream locations x/R = {-0.87, -0.53, -0.13, 0.13, 0.53, 0.87} were measured at phases θ = {0°, 45°, 90°, 135°}. At a given cross-stream location, several planes are measured in the y-axis and z-axis directions via the traversing system and stitched together. Due to time and storage constraints, not all phase and wake locations were measured in the same detail, with varying numbers of planes measured for each wake and phase pair. Further, due to the orientation of the cameras concerning the measurement planes, frequent masking operations are applied to the measurements to avoid shadows. Due to the placement of the PIV system, measurements focus predominately on the windward half of the cycle, reaching up to approx. y/R = -0.53.

3. Results and discussion

3.1. Baseline turbine performance

Before drawing conclusions about the induction field of the X-Rotor, the thrust vectoring of the scaled model must be discussed. The resolved thrust vectoring and thrust magnitude of the X-Rotor at a constant tip-speed ratio of $\lambda = 4.0$ is shown in Figure 3 averaged over a total of 250 cycles. The acquisition and transformation of the voltage signals from the load cells to dimensional forces are described in detail by LeBlanc et al. [14]. The final signals are filtered using a band-pass filter below 4Hz and above 10Hz. Finally, the loads are binned into $\theta = 5°$ segments. The behavior of the thrust is consistent with vertical-axis wind turbine performance

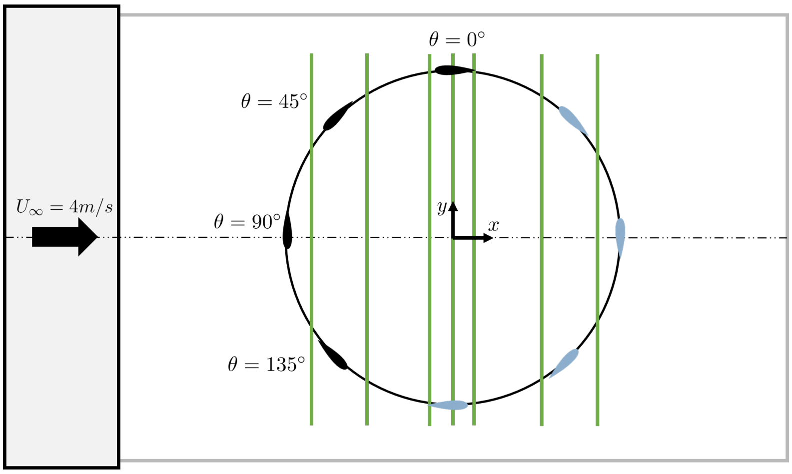

Figure 2: Scaled schematic of the top view of the setup. Blade 1 (black) phases are shown along with the respective positions of Blade 2 (blue). The measurement planes (green) are marked. The size of the airfoil cross-sections is not to scale.

and previous results reported by LeBlanc et al. [14]. The thrust in the freestream direction ($C_{T,x}$) is maximum at phases around $\theta = 90°$ and 270° when the two blades are in the furthest upwind and downwind positions. The peak magnitudes for both blades are C_T= 0.6 indicating a well-balanced system and turbine loading. The response in the radial direction ($C_{T,y}$) peaks with a 90° phase lag. Consistent with previous works and theory, the peak magnitudes are lower, around $C_{T,y} = \pm\ 0.17$. The resulting thrust magnitude is shown in Figure 3b and is driven mainly by the streamwise thrust ($C_{T,x}$) behavior, with maxima occurring close to $\theta =$ 90° and 270°.

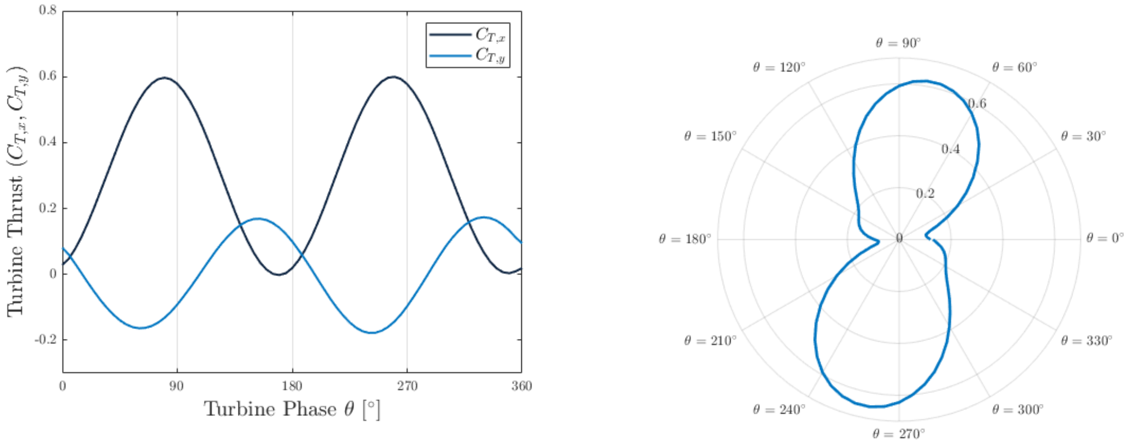

(a) Turbine thrust coefficient in the streamwise ($C_{T,x}$) and axial direction ($C_{T,y}$). The average standard deviation in $C_{T,x}$ and $C_{T,y}$ are 0.01.

(b) Turbine thrust magnitude $\sqrt{{C_{T,x}}^2 + {C_{T,y}}^2}$

Figure 3: Turbine thrust vectoring as a function of azimuthal position. All results are non-dimensionalized using the streamwise velocity U_∞ = 4m/s and a turbine frontal area of A= 1.29m^2.

3.2. Phase-locked flow fields at $\theta = 90°$

The phase-locked flowfields at $\theta = 90°$ at streamwise location x/R=-0.13 are summarized in Figure 4. The normalized flow fields in the streamwise (U_x), axial (U_z), and radial (U_y) directions are shown along with the normalized streamwise vorticity (ω_x).

As these measurements are taken within the volume of rotation of the rotor, the wake has not yet expanded, and it is contained within the bounds of the shed vorticity of the blades, evident in Figure 4a and Figure 4d. Characteristic of VAWTS, there is a clear presence of both shed-vorticity, and tip-vorticity [15, 16] stemming from both blades at the top and bottom of the rotor, labeled as B1 (at $\theta = 90°$) and B2 ($\theta = 270°$). The positions of these vortical structures are clearly visible in Figure 4d, with those created by B1 coinciding on the edge of the volume and those of B2 inboard at y/R=0.5 due to their convection downstream. Note that the structures appear more outboard of the swept area on the top blades due to the deflection of the cantilevered nature of the blades and centrifugal forces. The shed vorticity of B2t and B2b appear in an extremely curved shape which is an artifact of the difference in convective time between spanwise locations of the coned blade and streamwise plane.

Considering Figure 4a, there are several variations in the streamwise flow deficit across the frontal area of the rotor. As noted above, local deficits due to the tip and shed vorticity of the blades are present. Additionally, there is a clear asymmetry in the wake with higher magnitudes of flow deficit present on the windward side of the cycle ($y/R > 0$) compared to the leeward side ($y/R < 0$). This is highlighted by the presence of streamwise flow on the order of $U_x/U_\infty = 0.9$ in both the upper and lower halves of the rotor.

The radial velocity contour in Figure 4c follows the average expansion of the wake with minor variations imposed by the shed and tip-vorticity of the blades. The impact of the coned blades is once again visible along the shed vorticity path of B2, imposing variations in the expansion rates of the wake. However, a counteraction to the average expansion of the wake in the axial direction is visible in Figure 4b, where there is a presence of a downwash on the upper half of the rotor ($z/R > 0$) and upwash on the lower half ($z/R < 0$). Large local variations in the average expansion are imposed by the curved vortical structures from B1 and B2 in both the windward and leeward halves of the cycle. The impact of the axial induction imposed by the vorticity and blade loading is visible in the deformation of the wake near the tip regions in Figure 4a.

3.3. Flow field variation with phase

The discussion provided in Section 3.2 gives an overview of the phase-locked flowfield at the fixed cross-steam location. However, several phases need to be compared to make observations of temporal variations in the wake. The phase-locked flowfields at $\theta = 0°$, 45°, and $\theta = 135°$ are presented in Figure 5 (the case of $\theta = 90°$ is shown in Figure 4). The results include the normalised streamwise flow, axial velocity, and streamwise vorticity.

At a phase $\theta = 0°$, Blade 1 has yet to pass the upwind plane, and hence only the presence of strong vortical structures generated by Blade 2 are visible (Figure 5c). However, weak vortical structures shed by the tip region of Blade 1, which have convected and diffused downstream from the previous cycle, are also visible. The vortical structures of Blade 2 are near the edge of the frontal area where Blade 1 is passing, suggesting the presence of blade-vortex interactions. Consequently, local variations induced by these structures in the axial flow can be seen in Figure 5b. Regions of upwash and downwash in both the upper and lower half of the rotor suggest local regions of axial expansion and contraction. Given these axial variations and the streamwise deficit in the wake, the quivers confirm a radial wake expansion due to the continuity.

With two co-rotating closely-spaced vortices (B1 and B2) in the upper and lower halves at $\theta = 45°$, the induced level of upwash and downwash in the lower and upper halves has increased in magnitude. Furthermore, vortical structures on the left side of the rotor ($y/R < 0$) stemming from the leeward quartile of the cycle are very visible.

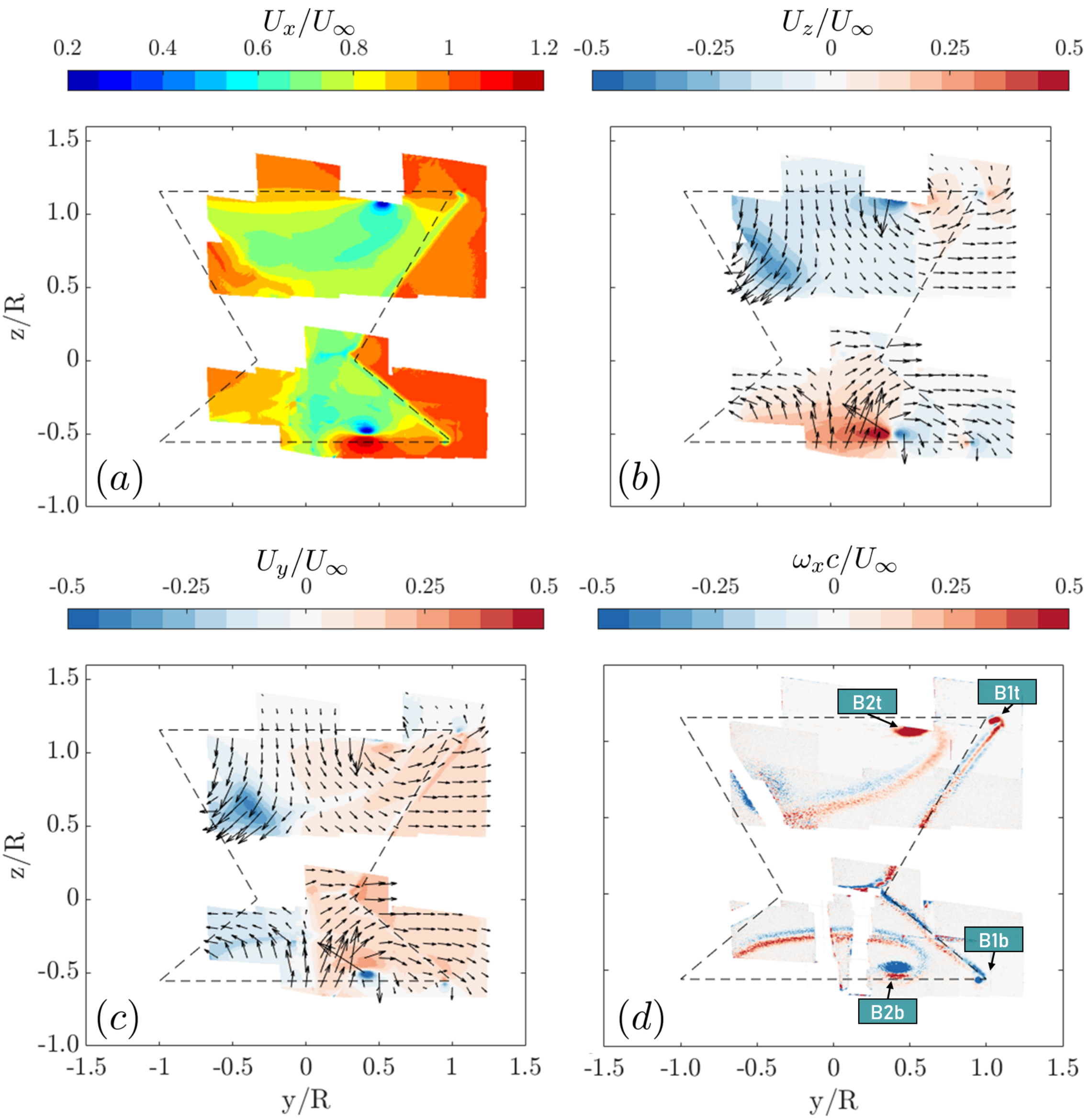

Figure 4: Flowfields at a streamwise location of x/R=-0.13 and phase-locked position of $\theta = 90°$. (a) Streamwise induction U_x/U_∞, (b) Axial induction U_z/U_∞, (c) Radial induction U_y/U_∞, (d) streamwise vorticity $\omega_x c/U_\infty$. Dashed lines indicate the frontal area of the X-Rotor perpendicular to the flow. Vortical structures produced by their respective blades are labeled, as described by Figure 1.

The case of $\theta = 135°$ at this cross-stream location is unique as we are slicing (or are just downstream) of the top tip-vortex shed by Blade 2 (B2t), as seen in Figure 5i. The entrance and exit of the vortex from the measurement plane are evident from the streamwise velocity component (Figure 5g) given the large, closely spaced areas of flow deficits. As we are downstream of the vortex, there is a large region of induced downwash in the upper half, with entrance and exit areas bound by the respective regions of upwash. Although the shed vorticity of the bottom blade (B2b) is visible, the tip vortex of the same magnitude in the upper half is not. This can be attributed to the larger deflection of the upper blades (and hence the difference in convective distance between the plane and the upper and lower blades) as well as the induction of the tower.

When evaluating the streamwise wake in consecutive temporal order across Figure 5 and Figure 4, a consistent asymmetry in the wake can be observed, where a heavier flow deficit is present on the right side of the rotor ($y/R > 0$). Consistent with results and observations by Tescione et al. [15], this wake asymmetry is driven by cyclic loading of the blades experienced in the windward and leeward quarterlies of the flow as well as the subsequent co-rotating and counter-rotating vortical pairs.

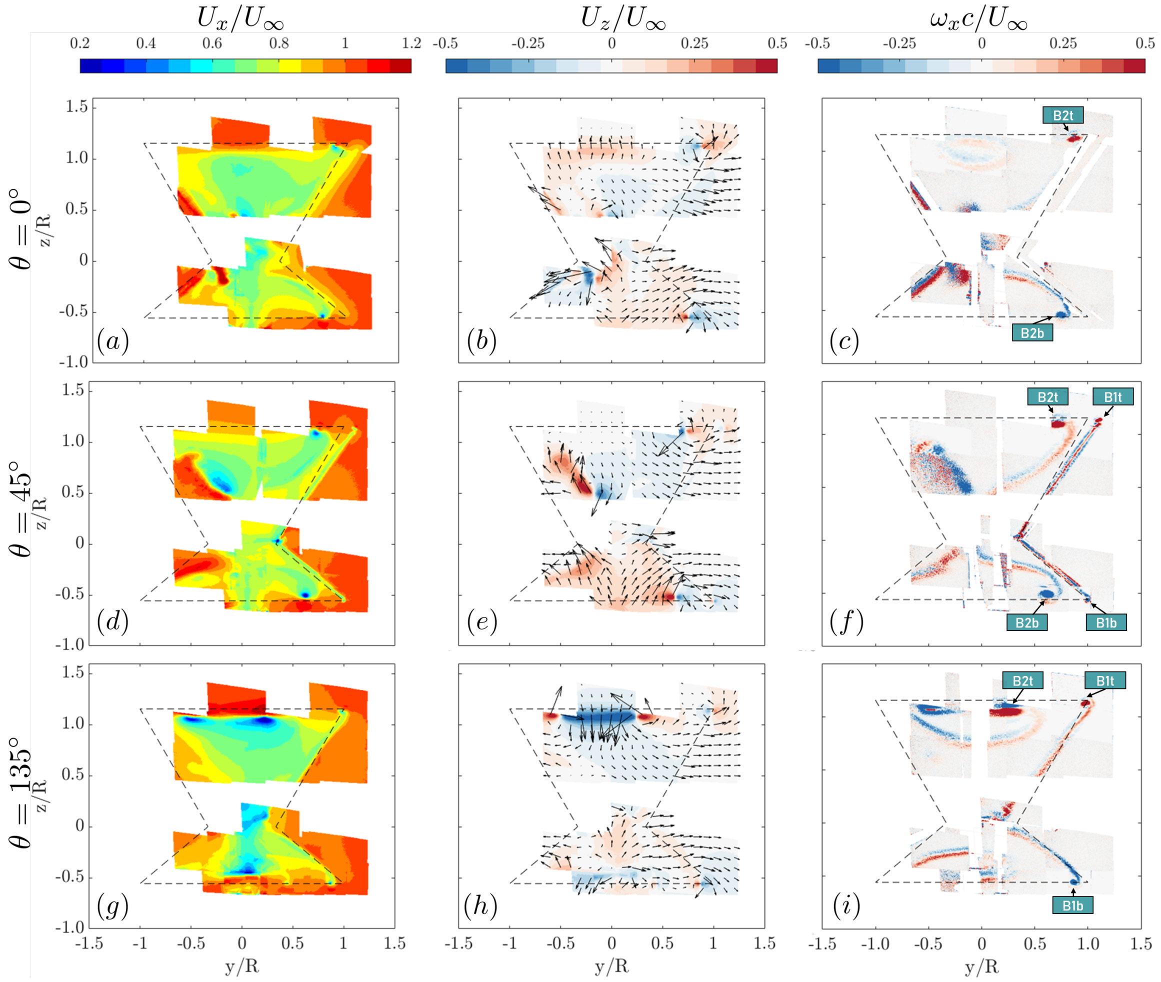

Figure 5: Normalized streamwise velocity U_x/U_∞, axial velocity U_z/U_∞, and streamwise vorticity $\omega_x c/U_\infty$ at a phase-locked position of $\theta = 0°$ (a-c), $\theta = 45°$ (d-f) and $\theta = 135°$ (g-i)streamwise. All results are at cross-stream location x/R=-0.13. The dashed lines indicate the frontal area of the X-Rotor perpendicular to the flow.

3.4. Spacial evolution of the wake

The results in Section 3.2 and Section 3.3 focused on the phased-locked measurements at x/R= -0.13 and illustrated a strong presence of axial induction component imposed by the tip and shed vorticity of the coned blades across several phases. These effects on the wake are further explored on an extended set of upstream and downstream locations shown in Figure 6.

Starting from the most upstream position, the wakes at x/R = -0.87 depicted in Figure 6a shows a large local velocity deficit in the areas surrounding the tip-vortex of Blade 1. As

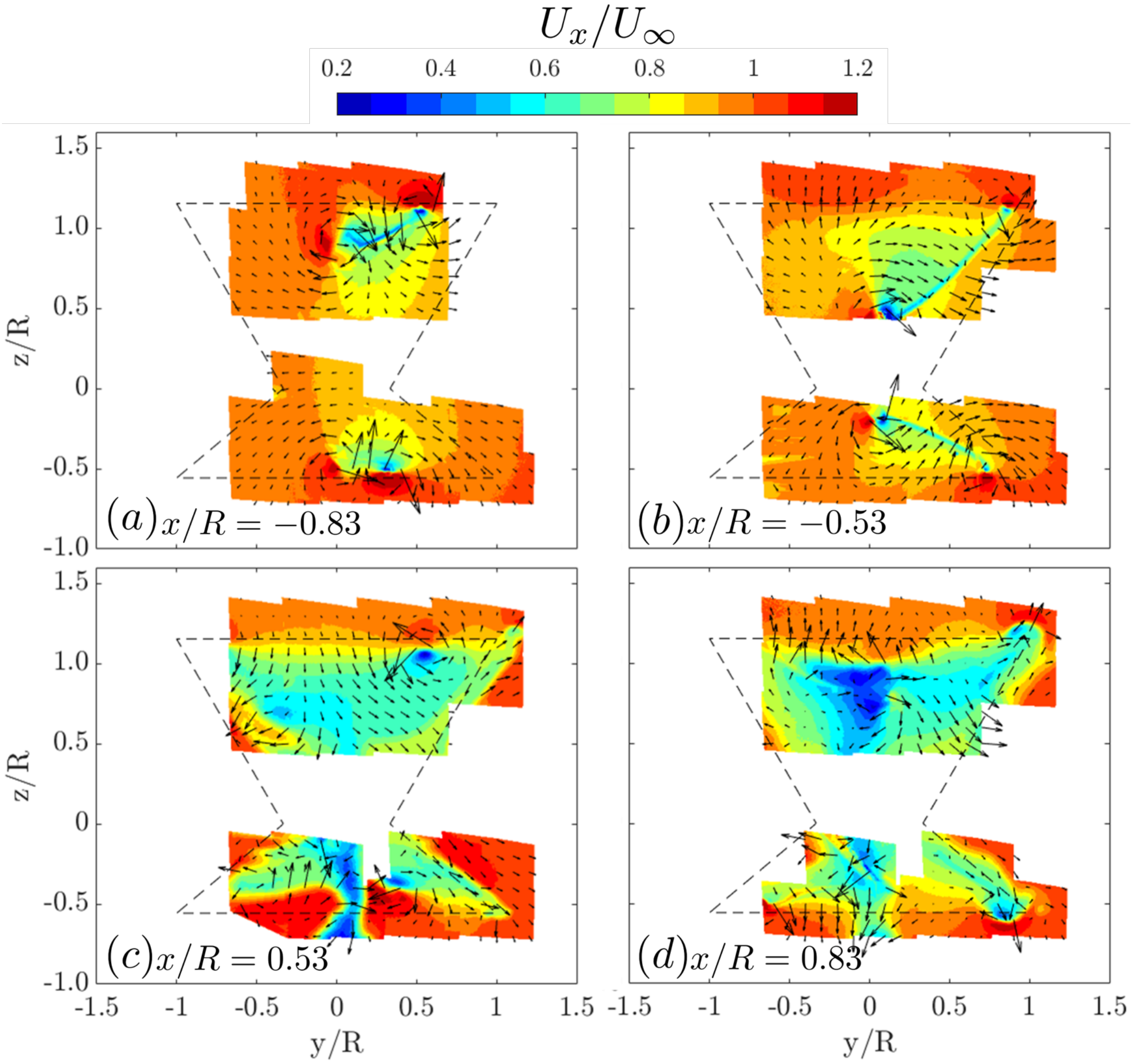

Figure 6: Normalized streamwise velocity U_x/U_∞ at a phase-locked position of $\theta = 90°$ and streamwise locations (a) x/R=-0.87, (b) x/R=-0.53, (c) x/R= 0.53, and (d) x/R= 0.87. The dashed lines indicate the frontal area of the X-Rotor perpendicular to the flow.

this plane is not yet at the tip, there is still a clear flow deficit due to the shed vorticity of the blade. Consistent with the results discussed in Section 3.2, there is a large variation in streamwise velocity when moving along the span at a given y/R location due to the varying distances between the blade and plane location. More of the velocity deficits caused by B1t and B1b become present when moving further downstream to the location x/R=-0.53, shown in Figure 6b. A strong gradient in the streamwise flow velocity is evident both along the span of the blade as well as in the axial direction, ranging from $U_x/U_\infty = 0.6$ to 0.9 at z/R= 0.6 and 1.1, respectively.

The flowfields presented in Figure 6c and Figure 6d are in the downstream half of the turbine. The wake imposed by the tower is present at x/R=0.53 before recovering slightly in x/R=0.87. Similar to Figure 4a, there are axial variations in the streamwise flow imposed by the local vorticity structures and varying convective times to spanwise locations on the blade. When viewing the streamwise locations in consecutive order starting from Figure 6a, the impact of the axial tip-vorticity and subsequent axial induction on the contraction of the wake becomes more evident. This contraction is seen on both halves of the turbine but seems to be more severe on the lower half, as discussed in Section 3.3. The axial contraction is complemented by the radial expansion as suggested by the quivers across Figure 6c and Figure 6d.

4. Conclusions

In this work, the near wake of the X-Rotor vertical-axis wind turbine was investigated experimentally. Particle image velocimetry was used to capture the flow field at several phase-locked positions and streamwise locations within the rotor's volume of rotation.

Characteristic phenomena of vertical-axis wind turbines were observed for this novel geometry, including the presence of both tip and shed-vorticity as well as blade-vortex interaction. Due to the coned nature of the blades, the shed vorticity appears in an extremely elliptical shape when measuring at a plane perpendicular to the flow. These structures induce local variations in the average expansion of the wake across different phases. When comparing several cross-stream locations at a fixed phase in the wake, a gradual axial contraction and radial expansion can be observed. This process is driven by the tip and shed vortices in the near wake before convecting downstream and diffusing.

Future work will expand the analysis to all streamwise and phase combinations of the rotor to access the temporal variation in the wake. Further, the results will be compared and validated with numerical models and data from H-Type VAWT to further highlight the impact of coned blades on the near and far wake. The present results reveal a large potential for farm-scale installation due to the notable contraction and asymmetry of the wake, where even without any control methods streamwise flow on the order of $U_x/U_\infty = 0.9$ is already present within the volume of rotation. Planned experimental campaigns will investigate the impact of coned blades on the far wake using time-averaged results to confirm this favorable mixing process. Accelerated wake recovery could allow more tightly spaced rotors in a farm leading to higher power densities. Control strategies such as active and passive blade pitching will be investigated and would likely accelerate the wake recovery even more, making the X-Rotor a very promising candidate for a future large-scale installation.

5. Acknowledgments

The authors wish to acknowledge the funding received from the European Union's Horizon 2020 research and innovation program under grant agreement No 101007135.

References

[1] EC European Commission et al. "GREEN PAPER-a 2030 framework for climate and energy policies". In: *COM (2013)* 169 (2013).

[2] M. Dolores Esteban et al. "Why offshore wind energy?" In: *Renewable energy* 36.2 (2011), pp. 444–450.

[3] W. Tjiu et al. "Darrieus vertical axis wind turbine for power generation II: Challenges in HAWT and the opportunity of multi-megawatt Darrieus VAWT development". In: *Renewable Energy* 75 (2015), pp. 560–571.

[4] S. Mertens, G. van Kuik, and G. van Bussel. "Performance of an H-Darrieus in the Skewed Flow on a Roof". en. In: *Journal of Solar Energy Engineering* 125.4 (2003), pp. 433–440. DOI: `10.1115/1.1629309`.

[5] R. Whittlesey, S. Liska, and J. Dabiri. "Fish schooling as a basis for vertical axis wind turbine farm design". en. In: *Bioinspiration & Biomimetics* 5.2 (2010), p. 035005. DOI: `10.1088/1748-3182/5/3/035005`.

[6] J. Dabiri. “Potential order-of-magnitude enhancement of wind farm power density via counter-rotating vertical-axis wind turbine arrays”. en. In: *Journal of Renewable and Sustainable Energy* 3.4 (2011), p. 043104. DOI: `10.1063/1.3608170`.

[7] A. Buchner et al. “Dynamic stall in vertical axis wind turbines:scaling and topological considerations”. en. In: *Journal of Fluid Mechanics* 841 (2018), pp. 746–766. DOI: `10.1017/jfm.2018.112`.

[8] S. Jain and U. Saha. “The State-of-the-Art Technology of H-Type Darrieus Wind Turbine Rotors”. en. In: *Journal of Energy Resources Technology* 142.3 (2019). DOI: `10.1115/1.4044559`.

[9] D. T. Griffith et al. “A study of rotor and platform design trade-offs for large-scale floating vertical axis wind turbines”. In: *Journal of Physics: Conference Series*. Vol. 753. 10. IOP Publishing. 2016, p. 102003.

[10] W. Leithead et al. “The X-rotor offshore wind turbine concept”. In: *Journal of Physics: Conference Series*. Vol. 1356. 1. IOP Publishing. 2019, p. 012031.

[11] C. Flannigan, J. Carroll, and W. Leithead. “Operations expenditure modelling of the X-Rotor offshore wind turbine concept”. In: *Journal of Physics: Conference Series*. Vol. 2265. 3. IOP Publishing. 2022, p. 032054.

[12] L.E.M. Lignarolo et al. “Experimental analysis of the wake of a horizontal-axis wind-turbine model”. In: *Renewable Energy* 70 (2014), pp. 31–46.

[13] B. LeBlanc and C. Simao Ferreira. “Overview and design of pitchvawt: Vertical axis wind turbine with active variable pitch for experimental and numerical comparison”. In: *2018 Wind Energy Symposium*. 2018, p. 1243.

[14] B. LeBlanc and C. Simao Ferreira. “Experimental demonstration of thrust vectoring with a vertical axis wind turbine using normal load measurements”. In: *Journal of Physics: Conference Series*. Vol. 1618. 5. IOP Publishing. 2020, p. 052030.

[15] G. Tescione et al. “PIV-Based Analysis of 2D and 3D Flow Phenomena of Vertical Axis Wind Turbine Aerodynamics”. In: *32nd ASME Wind Energy Symposium*. 2014, p. 1080.

[16] C. Simão Ferreira et al. “Visualization by PIV of dynamic stall on a vertical axis wind turbine”. In: *Experiments in fluids* 46 (2009), pp. 97–108.